Vaporlike phase of amorphous SiO_2 is not a prerequisite for the core/shell ion tracks or ion shaping

H. Amekura,[1,*] P. Kluth,[2] P. Mota-Santiago,[2] I. Sahlberg,[3] V. Jantunen,[3] A. A. Leino,[3] H. Vazquez,[3] K. Nordlund,[3] F. Djurabekova,[3] N. Okubo,[4] and N. Ishikawa[4]

[1]*National Institute for Materials Science (NIMS), Tsukuba, Ibaraki, Japan*
[2]*Department of Electronic Materials Engineering, Research School of Physics and Engineering, Australian National University (ANU), Canberra, Australia*
[3]*Helsinki Institute of Physics and Department of Physics, University of Helsinki, Helsinki, Finland*
[4]*Japan Atomic Energy Agency (JAEA), Tokai, Ibaraki, Japan*

(Received 22 May 2018; published 4 September 2018)

When a swift heavy ion (SHI) penetrates amorphous SiO_2, a core/shell (C/S) ion track is formed, which consists of a lower-density core and a higher-density shell. According to the conventional inelastic thermal spike (iTS) model represented by a pair of coupled heat equations, the C/S tracks are believed to form via "vaporization" and melting of the SiO_2 induced by SHI (V-M model). However, the model does not describe what the vaporization in confined ion-track geometry with a condensed matter density is. Here we reexamine this hypothesis. While the total and core radii of the C/S tracks determined by small angle x-ray scattering are in good agreement with the vaporization and melting radii calculated from the conventional iTS model under high electronic stopping power (S_e) irradiations (>10 keV/nm), the deviations between them are evident at low-S_e irradiation (3–5 keV/nm). Even though the iTS calculations exclude the vaporization of SiO_2 at the low S_e, both the formation of the C/S tracks and the ion shaping of nanoparticles (NPs) are experimentally confirmed, indicating the inconsistency with the V-M model. Molecular dynamics (MD) simulations based on the two-temperature model, which is an atomic-level modeling extension of the conventional iTS, clarified that the "vaporlike" phase exists at $S_e \sim 5$ keV/nm or higher as a nonequilibrium phase where atoms have higher kinetic energies than the vaporization energy, but are confined at a nearly condensed matter density. Simultaneously, the simulations indicate that the vaporization is not induced under 50-MeV Si irradiation ($S_e \sim 3$ keV/nm), but the C/S tracks and the ion shaping of nanoparticles are nevertheless induced. Even though the final density variations in the C/S tracks are very small at the low stopping power values (both in the simulations and experiments), the MD simulations show that the ion shaping can be explained by flow of liquid metal from the NP into the transient low-density phase of the track core during the first ~10 ps after the ion impact. The ion shaping correlates with the recovery process of the silica matrix after emitting a pressure wave. Thus, the vaporization is not a prerequisite for the C/S tracks and the ion shaping.

DOI: 10.1103/PhysRevMaterials.2.096001

I. INTRODUCTION

When a swift heavy ion (SHI), i.e., a high-energy ion whose stopping processes in materials are mostly dominated by electronic interactions, penetrates certain materials, a cylindrical modified region called an ion track is formed. The diameter of the track is of the order of a few nanometers, while the length can be tenths of micrometers. The mechanism of the ion-track formation has been studied for a long time but is still under debate. Up to now, various models have been proposed: Coulomb explosion [1–3], inelastic thermal spike (iTS) [4–6], exciton self-trapping [7,8], and others.

Among them, the iTS two-temperature (TT) model is mostly applied to understand experimental results, because less well-known nonequilibrium processes in the subfemtosecond and subpicosecond regions are approximated by daily-life concepts such as heat diffusion and temperature. A pair of coupled heat-diffusion equations are solved:

$$C_e(T_e)\frac{\partial T_e}{\partial t} = \nabla \cdot [K_e(T_e)\nabla T_e] - G(T_e)(T_e - T_a) + A, \quad (1a)$$

$$C_a(T_a)\frac{\partial T_a}{\partial t} = \nabla \cdot [K_a(T_a)\nabla T_a] + G(T_e)(T_e - T_a), \quad (1b)$$

where C_i, K_i, $T_i (i = e, a)$; G; and A denote the specific heat, thermal conductivity, temperature of the electronic ($i = e$) and atomic ($i = a$) subsystems; electron-lattice coupling; and source term, respectively. Since $C_a(T_a)$ and $K_a(T_a)$ are generally inputted from experimental data measured mostly under *atmospheric pressure* in practical calculations, it is not clear whether this methodology is really applicable to the nonequilibrium "vaporizationlike" phenomena in ion tracks, where *high pressure* is expected due to a phase change in the confined track geometry. In this paper, we add quotation marks to the words like "vaporization," because it is not sure whether a well-defined liquid-vapor transition is possible in the nonequilibrium confined geometry. As described later, the existence of the "vaporlike" phase is confirmed by simulations.

*amekura.hiroshi@nims.go.jp

Recently the conventional iTS-TT approach has been improved by the two-temperature molecular dynamics (TT-MD) [9], where the atomic system is evolved by MD equation (2b) while the electronic system is evolved by the heat-diffusion equation (2a), i.e.,

$$C_e(T_e)\frac{\partial T_e}{\partial t} = \nabla \cdot (K_e \nabla T_e) - G(T_e)(T_e - T_a) + A, \quad \text{(2a)}$$

$$m_i \frac{\partial v_i}{\partial t} = F_i(t) + \xi m_i v_i, \quad \text{(2b)}$$

where $F_i(t)$ is the force on an atom i from the MD interatomic potential, and the second term of the right hand side of (2b) comes from the electron-lattice coupling. In this paper, we first tried to understand the experimental results from the conventional iTS-TT [Eq. (1)], but inconsistencies arose. Then we applied the TT-MD approach [Eq. (2)], as described in detail below.

Silica, an amorphous form of SiO_2, which consists of the most abundant elements in the earth's crust, i.e., oxygen and silicon, is an important material in numerous technologies: an excellent insulating material in silicon ultralarge-scale integration (ULSI) technology, a base material for optical fiber communication, etc. While it is perceived that irradiation with ions, including SHIs, is a powerful technique to tailor the shapes [10] and properties [11] of silica, the microscopic processes under ion irradiation in this material have not yet been fully understood in spite of its huge importance, particularly for SHI irradiation.

Kluth *et al.* have resolved the morphology of the ion tracks in silica using a combination of small angle x-ray scattering (SAXS) and TT-MD [12,13]. Since silica is amorphous, it is difficult to evaluate the tracks directly by transmission electron microscopy, except for very thin films [14]. They found that ion tracks in silica feature a cylindrical core/shell (C/S) structure, consisting of a lower-density core surrounded by a higher-density shell. Furthermore, they reported a dynamical consequence: If ion tracks of a hard-cylinder type could be formed, instead of the C/S type, the SAXS signal would disappear at high fluences. This is because the whole region was covered by the hard-cylinder tracks and would become homogeneous. It should be noted that SAXS is sensitive to nanosized density fluctuation. The experiments, however, showed that the SAXS signal did not disappear even at fluences as high as 3×10^{14} ions/cm^2, where a full coverage of the irradiated area by the tracks of about 50 times is expected [13]. MD simulations clarified that a new impact closer than 3 nm from the previous track centers annihilates the previous tracks [13]. This observation indicates that C/S tracks have never disappeared by overlapping of the tracks, but they exist under a dynamical balance between creation and annihilation of the C/S tracks by subsequent ion impacts.

The formation processes of the lower-density cores and the higher-density shells were presumed as following [12] according to the iTS-TT model represented by Eq. (1): At the central part of an ion track, the highest energy density is deposited. If the energy deposition is high enough, the temperature at the central part steeply rises, exceeding both the melting point and the boiling point. Due to the high temperature in the center, the volume expands; i.e., the density decreases. However, the periphery of the track, where the energy deposition is less, undergoes the melting but not the vaporization. The molten periphery is pressed by the "vaporized" core, and a higher density is attained. Then all the parts are quenched with an extremely high cooling rate, which is a typical characteristic of ion irradiation. Consequently, the core and shell parts were quenched while maintaining lower and higher density, respectively. Hereafter, this mechanism is called the vaporization-melting (V-M) mechanism.

A simple question arises: What kind of ion tracks are formed if the energy deposition is reduced so that the vaporization is inhibited? To answer this question, SAXS measurements and MD simulations have been carried out at a lower energy deposition level in this paper. With decreasing the energy deposition, the track structures become smaller and smaller. Consequently, we need to detect and calculate fine structures in the subnanometer region. It should be noted that Mota-Santiago *et al.* recently have proposed another mechanism for the C/S track formation without vaporization [15]; inhomogeneous temperature distribution along the radial direction that generates the C/S tracks.

This simple question is important not only for the fundamental understanding of the ion irradiation effects on silica, but also for the understanding of the mechanism of the ion shaping of metal nanoparticles (NPs) in silica [16–21]. The next section describes how important the C/S tracks are for the understanding of ion shaping.

II. MECHANISM OF THE ION SHAPING AND THE C/S TRACKS IN SILICA

Spherical metal NPs dispersed in silica elongate to the same direction parallel to the ion beam under SHI irradiation [16]. This phenomenon is called ion shaping and has received much attention for years. Up to now, two major mechanisms have been proposed: (i) synergy effects between ion hammering and NP melting [19], and (ii) thermal pressure via the C/S ion tracks [20]. Counterevidence of the former model is reported in Ref. [21]. In the latter model, the C/S tracks play an important role for NP elongation. If the V-M mechanism was correct, the vaporization of silica in the ion tracks would be a prerequisite for the ion shaping. In a previous paper [22], Amekura *et al.* studied the elongation efficiency of Zn NPs in silica under various SHI irradiations. The elongation efficiency was plotted against the electronic stopping power S_e as shown in Fig. 1. Simultaneously, the radii of the vaporization and the melting regions were calculated by Eq. (1) with the parameters shown in Table I. While both the vaporization and the melting of silica were confirmed under 200-MeV Au ($S_e = 17.7$ keV/nm) and 200-MeV Xe ($S_e = 15.0$ keV/nm), only the melting but not the vaporization was calculated under 60-MeV Ti ion irradiation ($S_e = 5.9$ keV/nm). However, the NP elongation was clearly observed even under the 60-MeV Ti irradiation, and even under 50-MeV Si irradiation ($S_e = 3.2$ keV/nm), where S_e is approximately half of that for the 60-MeV Ti ions.

Since the results of the iTS calculations depend on the parameters used, the missing of the vaporization under 60-MeV Ti irradiation ($S_e = 5.9$ keV/nm) could be a false result due to deviation of the parameters from the true values. It should

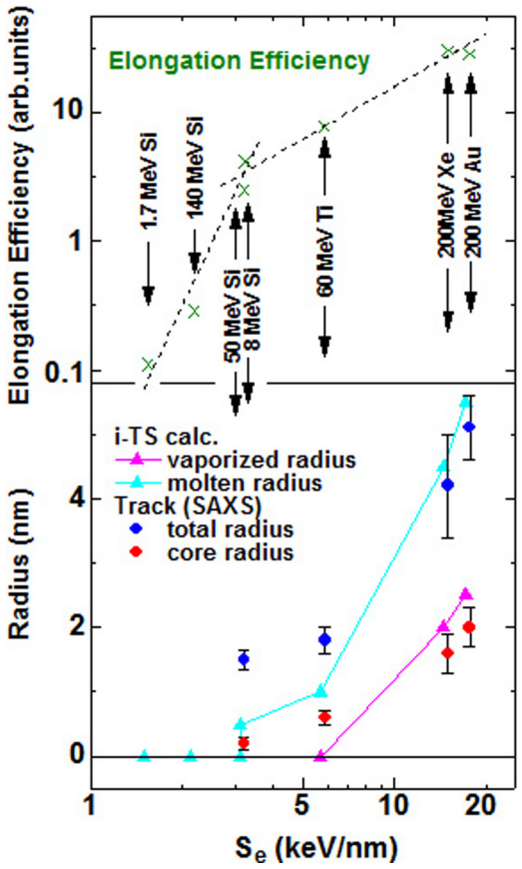

FIG. 1. Elongation efficiency for different ion/energy combinations of Zn NPs embedded in amorphous silica versus the corresponding ion-track dimensions and its corresponding comparison with the V-M model.

be noted, however, that we used the most reliable parameters which we know: i.e., the deviation is not so large. Consequently, even considering the parameter uncertainties, the vaporization under 50-MeV Si irradiation ($S_e = 3.2\,\mathrm{keV/nm}$) is highly unlikely, because the S_e is half of the value of 60-MeV Ti ions. These observations indicate that the NP elongation is induced without the vaporization under 50-MeV Si irradiation and probably 60-MeV Ti irradiation, which is inconsistent with the V-M model for the C/S track formation. In this paper, we have carried out SAXS measurements and shown that the C/S tracks are still observed even under conditions where the vaporization is not expected, indicating an inconsistency of the V-M model.

TABLE I. Parameters used for the inelastic thermal spike calculations in SiO_2.

Electronic thermal diffusion length λ (nm)	4.0
Latent heat of fusion (J/g)	142
Latent heat of vaporization (J/g)	4715
Melting point (K)	1972
Boiling point (K)	3323
Solid state mass density (g/cm^3)	2.26
Liquid state mass density (g/cm^3)	2.32

III. METHODS

A. Experiments

A total of 29 samples shown in Table II and more were evaluated with SAXS. Two types of a-SiO_2 were prepared, i.e., bulk silica of 0.5 mm thickness and a SiO_2 layer of 2 μm thickness on Si wafers. The bulk samples were from optical-grade silica glass of KU-1 type (OH > 1000 ppm). The 2-μm-thick SiO_2 layers were formed by thermal oxidation of Si wafers. SHI irradiations were carried out using the tandem accelerators at the Japan Atomic Energy Agency, Tokai Research and Development Center (JAEA-Tokai).

Synchrotron-based SAXS measurements in transmission mode were carried out at the SAXS/WAXS beamline of the Australian Synchrotron with a camera length of 960 mm and an x-ray energy of 11 keV. The scattering signal acquisition was carried out with the x-ray beam tilted by about 10° off the normal. Due to the high aspect ratio of the ion tracks, when tilted by 10° off normal incidence, an anisotropic scattering pattern is observed characterized by curved streaks [23]. An example of two scattering images is shown in Fig. 2. The arrows point to the curved streaks resulting from track scattering. The straight lines result from inelastic scattering of the silicon substrate supporting the thin silica films.

The high sensitivity to local electron density changes of SAXS allows us to correlate the characteristic scattering pattern with the corresponding morphology of the ion tracks for each sample. The amorphous nature of a-SiO_2 supports the presence of an angular symmetry. The analyzed scattering intensities were extracted using a selective mask of the streaks present in the anisotropic scattering pattern accompanied by a background subtraction of the region defined by a mask outlined perpendicular to the streaks.

B. Simulations

MD simulations on NP elongation in silica were carried out using the classical MD [24] code PARCAS [25–29], previously widely used to study radiation effects including swift heavy ions [26,30–32]. To initiate the ion track, we followed the practice of instantaneous energy deposition according to a profile obtained from the two-temperature iTS model [33]. This approach has been previously found to give good results in track radii [34] as well as elongation [31]. In this approach, all the atoms in the center of the material are given a certain amount of kinetic energy depending on their distance to the axis of the swift heavy ion passage. The energy deposition takes the form of some suitable increase in the velocity of the particles. The direction of the velocity increase can be given at random, by random number generators, and the sizes of the increments are calculated from the Maxwell-Boltzmann velocity distribution.

The NPs, whose elongation was to be studied, were chosen to be Au and Zn NPs. A sphere of 12 nm in diameter of fcc bulk gold was cut and compressed by 2%, following the procedure introduced in [35]. The compression was done because if two atoms are placed very near each other prior to the simulation, the immediate repulsion between them will be enormous. A cavity with the size and form of the original gold or zinc sphere was cut into a matrix of amorphous silicon

TABLE II. Samples evaluated by SAXS measurements: Ion irradiation conditions; the stopping power values at the surface of the samples are listed. The results of the SAXS measurements were described in the observation columns.

Sample code	Ion and energy	S_e@surf (keV/nm)	S_n@surf (keV/nm)	Substrate	Fluence (ions/cm^2)	Observation
VS-53	200-MeV Au	17.7	0.142	0.5-mm	1×10^{11}	Clear C/S pattern
VS-01	200-MeV Xe	15.0	0.051	SiO_2	1×10^{11}	Clear C/S pattern
VS-49	60-MeV Ti	5.9	0.011		1×10^{11}	No identified signal
VS-51					1×10^{12}	C/S pattern
VS-45	50-MeV Si	3.2	0.004		1×10^{11}	No identified signal
VS-47					1×10^{12}	?
VS-61	8-MeV Si	3.2	0.017		1.5×10^{12}	No identified signal
VS-41	140-MeV Si	2.2	0.001		1×10^{11}	No identified signal
VS-42					1×10^{12}	Possibly C/S pattern
VS-63	1.7-MeV Si	1.6	0.055		1.5×10^{12}	No identified signal
TF-31	60-MeV Ti	5.9	0.011	2-μm SiO_2/Si	1×10^{11}	No identified signal
TF-32					3×10^{11}	Weak C/S signal
TF-33					1×10^{12}	C/S pattern
TF-34					3×10^{12}	C/S pattern
TF-01	50-MeV Si	3.2	0.004		1×10^{11}	No identified signal
TF-02					3×10^{11}	No identified signal
TF-03					1×10^{12}	No identified signal
TF-04					3×10^{12}	Possibly C/S pattern
TF-05					1×10^{13}	C/S pattern
TF-06					3×10^{13}	C/S pattern
TF-07					1×10^{14}	C/S pattern
TF-17	8-MeV Si	3.2	0.017		1×10^{11}	No identified signal
TF-18					3×10^{11}	No identified signal
TF-19					1×10^{12}	No identified signal
TF-20					3×10^{12}	No identified signal
TF-21					1×10^{13}	Extremely weak signal
TF-22					3×10^{13}	Weak C/S signal
TF-15	1.7-MeV Si	1.6	0.055		1×10^{13}	No identified signal
TF-16					3×10^{13}	No identified signal

dioxide (a-SiO_2), into which the compressed metal NP was then placed. This system was kept under pressure control at 300 K, allowing the whole structure to reach equilibrium. During this time, the compressed sphere expanded into the cavity, simultaneously interacting with the a-SiO_2 structure around it and establishing natural distances between all atoms in the system.

The interatomic potentials for the Au-SiO_2 system were the same as in Ref. [31]; i.e., an embedded-atom-method-like potential was used for Au [36,37], and the Watanabe-Samela potential for SiO_2 [38,39]. For the system with Zn NPs, we used the Tersoff-like Munetoh potential for SiO_2 [40] combined with the Tersoff-like Zn potential from [41]. To systematically examine how the amount of incoming energy affects the elongation when everything else remains the same, for the Au NP cases, the energy deposition in the surrounding SiO_2 was modified by linear scaling from the profile used in [31]. For both Au and Zn NP cases, we also simulated SHI irradiation events for the 50-MeV Si, 60-MeV Ti, and 200-MeV Xe projectile ions, which had been included in the experiments described above. The two initial state situations for the simulations of Au and Zn differed only in the initial structures of the material from which the metal sphere was cut and then compressed.

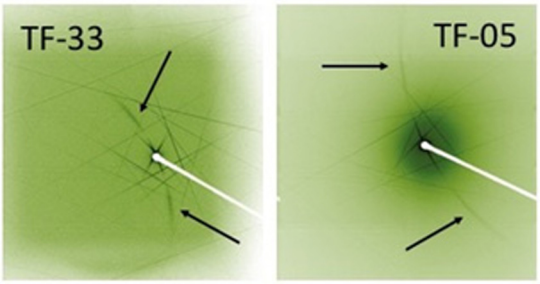

FIG. 2. SAXS scattering images of ion tracks in two silica samples. The arrows point to the curved streaks resulting from track scattering.

In the analysis of the data, we examined the dependence of the elongation effect on the energy deposited by the SHI. The time for all simulations was 100 ps; there was no need to choose a longer simulation time, since the simulated systems do not change significantly during the latter half of the simulation. We also investigated the density distribution of the SiO_2 above and below the NPs, in and around the formed ion track. These density variations proved to be of key importance for the mechanism behind the observed elongation. The simulation cell was divided into cylindrical shells of width 1 nm, and the radial distribution of the density was analyzed by comparing the values for the different shells.

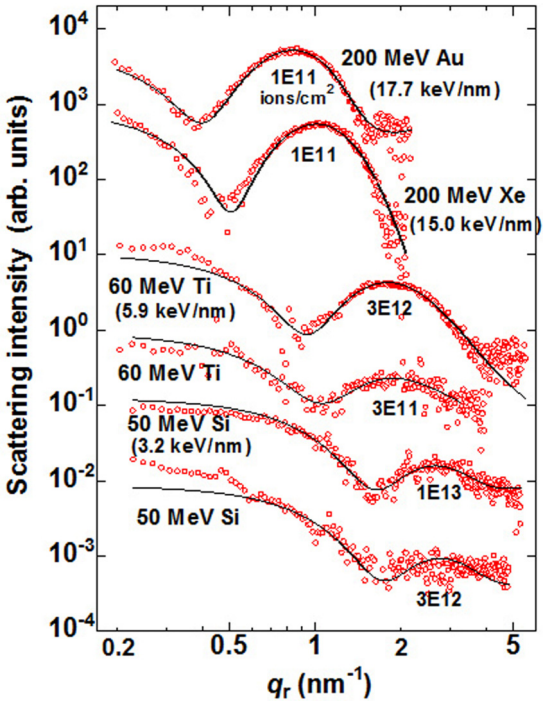

FIG. 3. Integrated SAXS intensities along the scattering vector q_r of amorphous silica samples irradiated with different ion/energy/fluence combinations. Circles show the experimental results and the solid lines represent the numerical fit considering a C/S model. The data are offset for clarity.

IV. EXPERIMENTAL RESULTS

Small angle x-ray scattering

Figure 3 shows the one-dimensional scattering intensities (circles) as a function of the scattering vector q_r, which contains the information about the radial density distribution in the tracks. In this work, the best fit to the extracted data for all samples was obtained assuming a cylindrical C/S geometry [13]. The scattering amplitude for this model can be expressed as

$$f(q) = \frac{2\pi L \rho_s}{q_r}\left[R_T J_1(q_r R_T) - \left(1 - \frac{\rho_c}{\rho_s}\right) R_c J_1(q_r R_c)\right], \tag{3}$$

where L corresponds to the ion-track length; ρ_c and ρ_s are the density change (scattering contrast) with respect to the bulk material of the core and shell region, respectively. The term R_T corresponds to the total ion-track radius ($R_T = R_c + T_s$) and J_1 is the first-order Bessel function. The resulting integrated scattering intensity can be expressed considering a narrow Gaussian distribution of the track dimensions:

$$I(q_r) \propto \int \frac{1}{\sqrt{2\pi}\sigma} \exp\left[-\frac{(r_i - R_i)^2}{2\sigma^2}\right] |f(q_r)|^2 dr_i. \tag{4}$$

The distribution is considered around the track core radii ($r_i = r_c$) with a mean value R_c, while the distribution of the shell thickness (t_s) is fixed by scaling the distribution in r_c to T_s/R_c. The size distribution for the track dimensions arises from small deviations of the tracks from monodisperse cylinders due to variations in electronic stopping power. With our SAXS setup, we measure approximately 10^7 tracks such that the results provide an average over this number of tracks. However, given that all tracks are generated from identical ions, the radial density in the tracks can be expected to only vary minimally between tracks. The fits to the model are shown as solid lines in Fig. 3 and show excellent agreement with the data. The fitted values are listed in Table III. Fittings with the hard-cylinder model were also attempted but unsuccessful.

The extracted scattering patterns of all samples clearly resemble that of a C/S structure. The negative values of the density ratio, ρ_s/ρ_c, imply that an underdense core surrounded by an overdense shell compared to unirradiated material or vice versa is present. The former has been confirmed previously by [12]. In the case of samples irradiated with ion/energy combinations corresponding to S_e values near the threshold of ion-track formation (~2 keV/nm [11]), the local minima and maxima are shifted towards higher q_r values, a clear signal of scattering objects of smaller dimensions. The observed SAXS scattering intensity depends on the number and volume of the scattering objects, as well as their corresponding scattering contrast or local density change; hence, in the low electronic stopping power regime, the corresponding ion tracks show a lower scattering intensity due to their smaller size and possibly smaller density change. Thus, a higher fluence (or number of tracks) to successfully observe the scattering signal of the tracks in amorphous silica samples irradiated with low S_e is required, where the fluence required varies from one to even two orders of magnitude above the values commonly considered for higher-energy cases.

TABLE III. Ion irradiation parameters including electronic energy loss S_e, as calculated by SRIM2008, fitted parameters from SAXS measurements: R_c (inner core radius), T_s (shell thickness), and R_T (total ion-track radius). Also calculated is the total area in percent covered by ion tracks and the overlap area with respect to the track covered area.

Sample code	Ion and energy (MeV)	Fluence ($\times 10^{12}$ cm^{-2})	S_e (keV/nm)	R_T (nm)	R_c (nm)	T_s (nm)	Polydispersity (nm)	Density change ratio (ρ_c/ρ_s)	Covered area (%)	Overlap (%)
VS-53	200 Au	0.1	17.7	5.1 ± 0.2	2.0 ± 0.3	3.1 ± 0.2	0.3 ± 0.2	−2.5 ± 0.6	7.8	4.1
VS-01	200 Xe	0.1	15	4.3 ± 0.2	1.5 ± 0.1	2.8 ± 0.3	2.4 ± 0.1	−3.0 ± 0.7	5.6	2.9
TF-32	60 Ti	0.3	5.9	1.3 ± 0.4	0.3 ± 0.1	1.0 ± 0.4	0.2 ± 0.2	−5.5 ± 4.5	1.6	0.8
TF-33	60 Ti	1.0	5.9	2.0 ± 0.2	0.5 ± 0.1	1.5 ± 0.1	0.2 ± 0.1	−5.2 ± 1.1	11.8	6.4
TF-04	50 Si	3.0	3.2	1.5 ± 0.1	0.2 ± 0.1	1.3 ± 0.1	0.1 ± 0.1	−15.8 ± 1.4	19.1	10.9
TF-05	50 Si	10.0	3.2	1.8 ± 0.2	0.2 ± 0.1	1.6 ± 0.2	0.2 ± 0.2	−4.5 ± 1.0	63.8	59.4

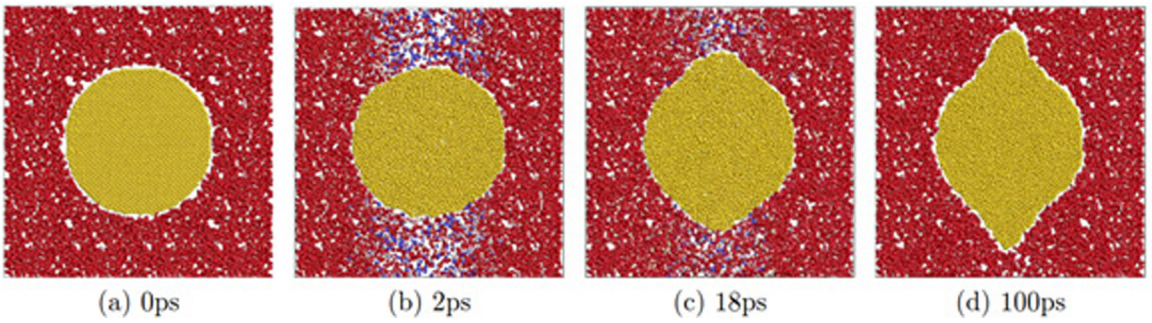

FIG. 4. Illustration of elongation in a Au NP irradiated with 200-MeV Xe ions. The figure illustrates how around 2 ps, an underdense track forms along the ion path, into which material from the molten metal nanoparticle then flows on timescales exceeding 10 ps.

To assess if overlap effects become important at higher irradiation fluences F, we follow the same overlap model ($d = 1 - \exp[-\pi R_T^2 F]$) as in [12]. The values for the percentage of area covered with tracks as well as the percentage of track overlap with respect to the covered area are listed in Table III. The overlap is small except for the highest fluence. However, for the samples irradiated with 60-MeV Ti and 50-MeV Si ions, the shapes of the scattering curves are almost independent of the fluence (i.e., only the intensity changes), indicating no intertrack scattering (structure factor) becomes important at these fluences; i.e., the tracks can be viewed as independent scattering objects. When track overlap becomes important, a change in the shape of the scattering curves becomes apparent [13]. The absence of a structure factor is also consistent with the stochastic distribution of the tracks during the irradiation process.

The total radii and the core radii of tracks determined from SAXS analysis are compared with those of transiently vaporized or molten regions of tracks determined from the iTS calculations as shown in Fig. 1. While the iTS calculations reproduce well the radii determined by SAXS for high-S_e irradiations (>10 keV/nm), the calculations underestimate the radii for low-S_e irradiations (3–5 keV/nm).

It should be noted again that while we have evaluated 29 different conditions of irradiations as shown in Table II, we have *always* observed the C/S structures of tracks unless the signals from the tracks are too weak to be fitted. No hard-cylinder structures of tracks have been observed.

V. ATOMISTIC SIMULATIONS

The results from MD simulations for Au NPs are illustrated in Figs. 4–6. The results show that, as expected from previous works [31], for high-energy ions such as 200-MeV Xe, the elongation proceeds by flow of molten metal into the underdense track core (Fig. 4).

To derive a conclusion on possible transient phase states right after the impact, we analyzed the pair correlation function $g(r)$ for the atoms within the hot region of the tracks formed by 50-MeV Si and 200-MeV Xe ion impacts. In Fig. 5(a), we show the comparison of pair correlation functions for SiO_2 structure before and after 5 ps from the impact by Si and Xe ions, respectively. We see that in all three cases, the first peak is strongly pronounced, while the second peak, indicating amorphous structure of the pristine structure, becomes less prominent with increase of the ion energy.

To obtain a point of comparison for whether or not this situation corresponds to a liquid or highly pressurized vapor phase of SiO_2, we performed additional equilibrium simula-

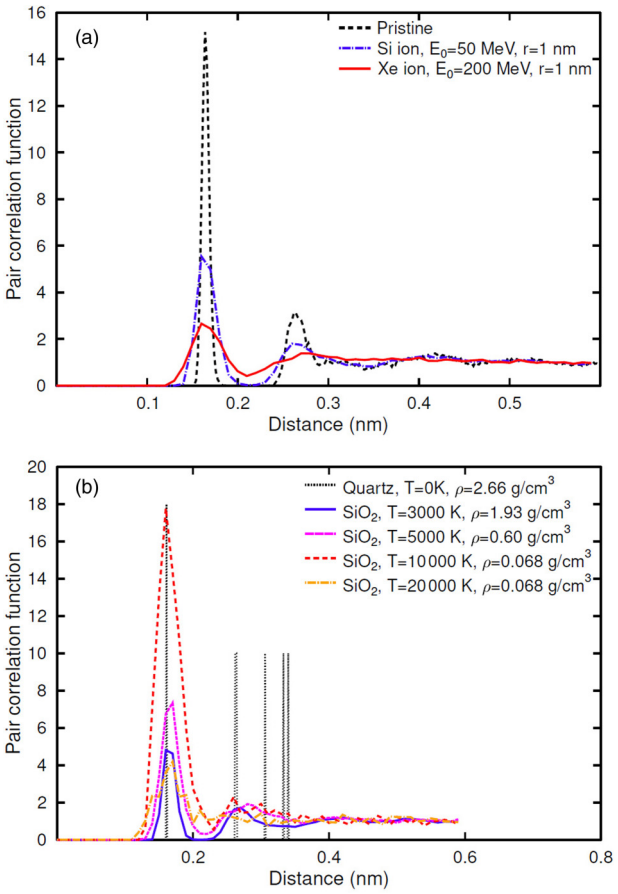

FIG. 5. Pair correlation functions, $g(r)$, for SiO_2 structure: (a) within the cylinder of the radius 1 nm before the impact and right after 50-MeV Si and 200-MeV Xe ions deposited energy to the lattice; (b) after a SiO_2 cell was equilibrated at zero pressure (except for 20 000 K) and the corresponding temperature shown in the legend. $g(r)$ is normalized by the number of atoms found on average in each spherical shell *rdr* according to the actual density of the simulation cell. The highest peak at 10 000 K indicates the presence of small clusters in the vapor phase, which disappear at even higher temperature of 20 000 K. The peaks of the quartz structure are shown intentionally equal, as they are used to guide the eye for the coordination peak in crystalline SiO_2.

tions for SiO_2 for underdense molten and vaporized phases. In these simulations, an initial quartz cell with 1350 atoms was shock-heated to 15 000 K; then it was allowed to evolve under pressure and temperature control to different target temperatures. Each case was run until the pair correlation function was stabilized. These results are shown in Fig. 5(b). In all cases up to 10 000 K, we observe a clear first-nearest-neighbor peak, showing that the SiO dimers are quite stable and exist even in the vapor phase (at least in this interatomic potential and the MD timescale of about 100 ps). At 3000 K, the pressure was relaxed at the density of 1.9 g/cm^3 and the results show a clear second-nearest-neighbor peak, which indicates that at this temperature, the SiO_2 is in a liquid (molten) phase. At the temperatures of 5000 and 10 000 K, the first-nearest-neighbor peak is strong, but the second-nearest-neighbor peak is not distinct anymore (there is no dip after it), indicating that this phase can be considered a vaporlike phase. In the 20 000 K case (intentionally created with a fixed simulation cell size to have the same density as the 10 000 K case), finally the first-nearest-neighbor peak is weaker, and there is no feature at all around the second-nearest-neighbor peak.

Comparing Figs. 5(a) and 5(b), we conclude that 50-MeV Si ions deposit energy into a track sufficient to achieve melting of SiO_2 structure under high pressure (the second peak is still clear). The pair correlation function obtained for the atoms in the track of the 200-MeV Xe ion is much closer in shape to the curve obtained for 10 000 K temperature in the thermally equilibrated SiO_2, which corresponds to a "vapor" phase at zero pressure. In particular, the Xe ion pair correlation function does not go to zero after the first-nearest-neighbor peak and has a second-nearest-neighbor peak, which would be clearly distinguished, similar to the reference 10 000 and 20 000 K vapor pair correlation functions. Hence, we conclude that the high-energy Xe ions indeed are able to vaporize SiO_2. These hot atoms with the average energy of ∼1.5 eV/atom (corresponding to ∼12 000 K), cause a rapid expansion outwards from the track center, generating pressure waves, which are eventually responsible for the formation of a C/S structure. The energy of atoms in the 50-MeV Si ion track is lower (only ∼0.5 eV/atom). The corresponding pair correlation function is similar in shape to the molten phase at 3000 K [see Fig. 5(b)]; i.e., there is no vaporlike phase formed. However, also in this case, the thermal expansion within the track is able to generate weaker pressure waves, transiently reducing the density within the track, which is sufficient to cause a slow flow of metal atoms, i.e., the ion shaping.

The new time-dependent analysis of the ion shaping (Fig. 6) shows that the elongation timescale (red curve) matches essentially perfectly the timescale of when the track core density is underdense and changing (green and blue

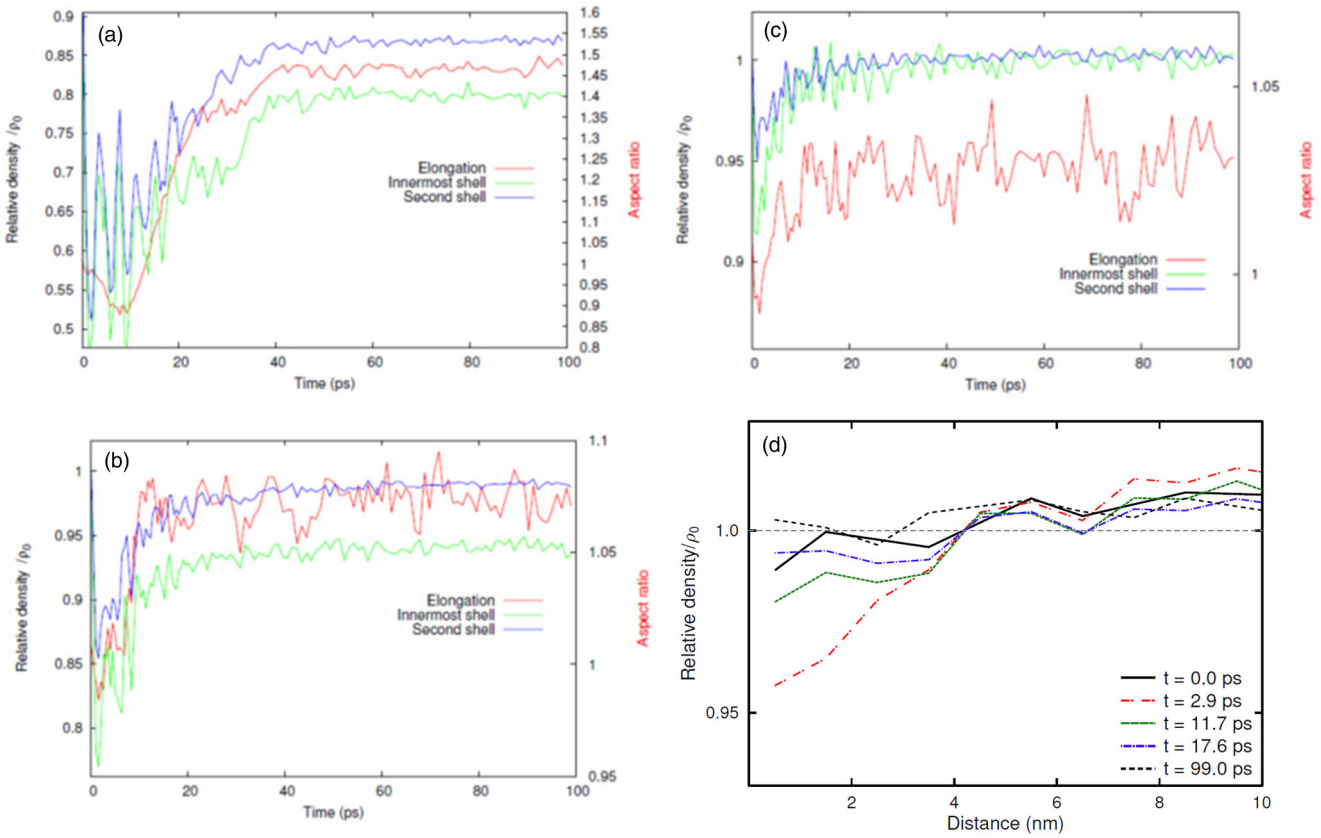

FIG. 6. Illustration of the time dependence of the track formation and elongation in a Au NP in SiO_2 irradiated with (a) 200-MeV Xe ions, (b) 60-MeV Ti ions, and (c) 50-MeV Si ions. The red line and right-hand axis show the change of the Au nanoparticle aspect ratio with time, while the left-hand axis and green line show the density in the innermost 1-nm cylindrical shell around the ion path in SiO_2, and the blue line the density in the second 1-nm shell. Part (d) shows how the radial density profile was modified during the track evolution after a 50-MeV Si ion. The profiles are shown for different times between 0 and 99 ps.

curves). When the track core density stabilizes around 40 ps, the aspect ratio of the major to minor diameters of the nanoparticle also stops changing (the elongation stops). What is very noteworthy is that the same observation holds also for 60-MeV Ti and 50-MeV Si ions [Figs. 6(b) and 6(c)]. Although the ion-shaping effect is smaller and hence the statistical fluctuations larger, in these cases the timescale of the aspect ratio change also clearly correlates with the transient density changes in the track core. In both cases, the change in track core density and elongation stops at about 20 ps. The 50-MeV Si case is particularly interesting, since the final relative density change is very small at all separations (of the order of 1%, Fig. 6(d)], while there still is a clear elongation of about 3%. The results for Zn NPs [Fig. 7) show a clearly stronger elongation than in Au, which is expected since the melting point of Zn is much lower than that in Au. Also in these cases, the correlation between the transient underdensification and elongation timescale is very clear.

Figure 8 compares the final relative density in the innermost 1-nm cylindrical shell with the elongation as a function of stopping power. As shown in Table III, the stopping power S_e of 200-MeV Au ion in SiO_2 is 17.7 keV/nm, which is out of the scale of Fig. 8. Instead, the results for the runs with 200-MeV Au ions with stopping power scaled linearly down

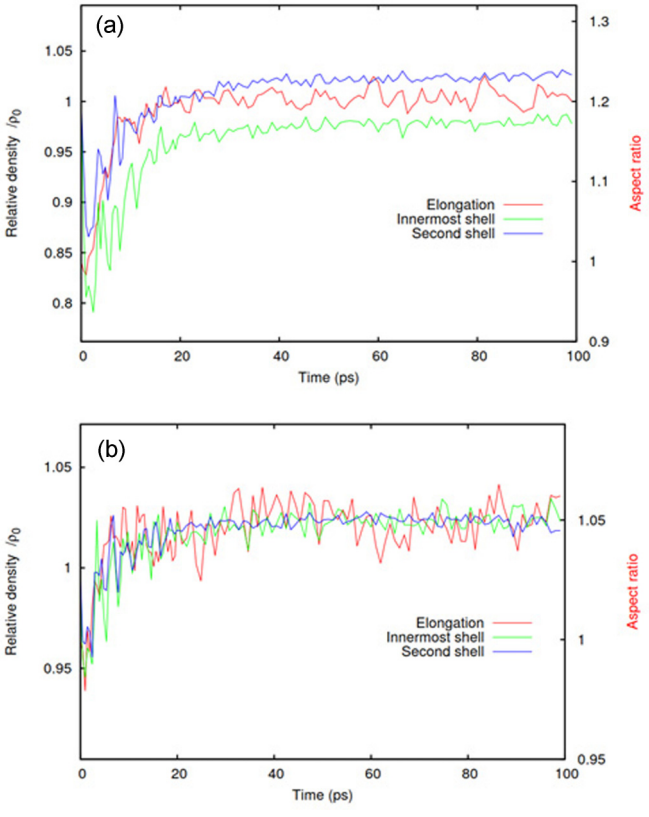

FIG. 7. Illustration of the time dependence of the track formation and elongation in a Zn NP in SiO_2 irradiated with (a) 60-MeV Ti ions and (b) 50-MeV Si ions. The red line and right-hand axis show the change of the Zn nanoparticle aspect ratio with time, while the left-hand axis and green line show the density in the innermost 1-nm cylindrical shell around the ion path in SiO_2, and the blue line the density in second 1-nm shell.

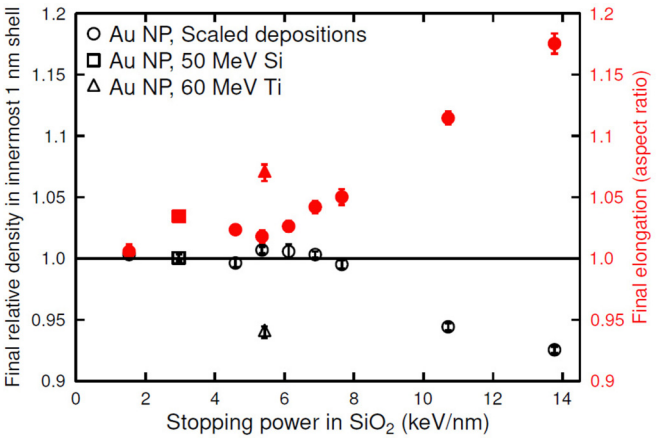

FIG. 8. Final relative density in the track core (open symbols) and Au NP elongation (closed symbols) as a function of stopping power. The results show that even when the final density change is less than 1%, the clusters can elongate by several percent. The error bars are one sigma errors of the average.

are shown. (Note that since the shape of the energy deposition profile is different for the 200-MeV Au, 50-MeV Si, and 60-MeV Ti ions, a perfect correlation with the same stopping power is not expected.) Consistent with the discussion above, one can clearly observe an ion-shaping elongation effect, even when the final density change in the track core is very small.

We ran additional simulations of multiple impacts of the 50-MeV Si ions on a Au NP (12 nm in diameter) embedded in a-SiO_2 to investigate the evolution of elongation of NP at higher fluences. At the end of each simulation, the Au NP, which undergoes a fast heating and quenching during the SHI impact, freezes its final shape in a metastable amorphous phase. We replace this shape with a crystal of the same shape and the same number of atoms as the actual NP. This procedure is motivated by recrystallization of Au NPs observed experimentally, where the time interval between two subsequent ion impacts onto a single NP can easily extend to a few seconds. As we showed in [31], the frozen SiO_2 structure around the Au NP prevents significant relaxation of the shape, while the amorphous phase has been fully replaced by a polycrystalline structure in a microsecond time interval.

In Fig. 9, we show the evolution of the aspect ratio of a spherical Au NP. The horizontal axis shows the subsequent number of ion impacts and the vertical axis is the aspect ratio of the NP. The snapshots of the NP after the first, fourth, and tenth impacts are shown for illustration purposes. Each image contains a circle outlining the shape of the original NP for reference. We clearly see that the elongation after the first impact is barely visible; however, after the tenth impact, it becomes well visible and prominent. It is also noteworthy that elongation occurs after every impact, which shows that the elongation is not a random event but occurs consistently.

VI. DISCUSSION

Figure 1 shows that the C/S track formation could be relatively well explained by the iTS-TT model and purely electronic energy loss at high-S_e regions, but not at the

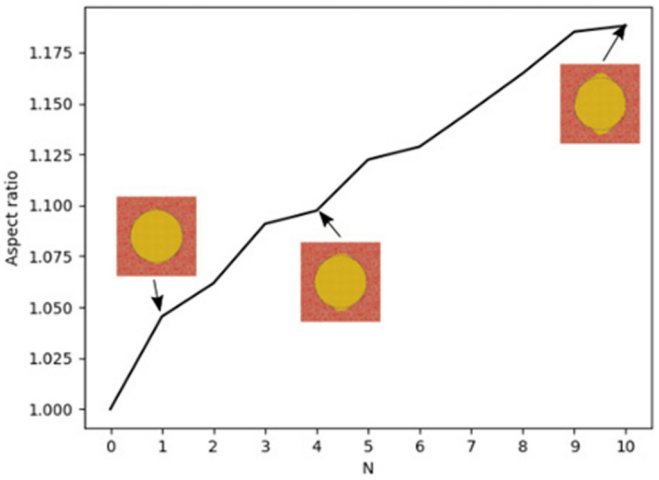

FIG. 9. Evolution of the aspect ratio of a 12-nm Au NP embedded into a-SiO_2 after subsequent impacts of Si ions with the energy of 50-MeV. The snapshots illustrate the evolution of the nanoparticle: barely visible elongation after the first impact becomes prominent after the tenth.

low-S_e region. Cooperation with other effects could possibly be expected to vaporize the track cores in the low-S_e region. Toulemonde *et al.* explained the track formation in silica under low-energy (0.5–15 MeV) heavy Au ion irradiation, where the track formation is not explained by S_e only, but the synergy of S_e and S_n [42]. However, this is not our case. While the S_n/S_e ratio was 0.31–4.5 for the cases of Toulemonde *et al.* [42] because of the *low energy* (<15 MeV) and the *heavy* Au ions, the S_n/S_e was 1.9×10^{-3} for 60-MeV Ti ions and 1.3×10^{-3} for 50-MeV Si ions, i.e., much lower for our cases. Even if the synergy effect is involved in our case, the contribution is negligible. Consequently, the C/S track formation at low-S_e irradiation cannot be explained by the synergy effect.

This conclusion is supported by the MD simulations, which do not include any recoils caused by nuclear stopping power at all, yet show both a track formation effect and ion shaping. They show instead that the track formation can be explained by the transient heating leading to flow of molten material into the track core. The time-dependent analysis done in this work shows that the molten metal flow correlates perfectly with the timescale when the track core is underdense and evolving. Since the transient track density can be much lower than the final one, it is possible to get an ion-shaping effect even when the final C/S density difference is very small. Moreover, the MD simulations for 50-MeV Si ions show [Figs. 6(c), 6(d), and 7(b)] that the density change in the track core is never more than 5% of the normal density. This is not consistent with a vaporization model, where one expects densities going down by 100%. A detailed analysis of pair correlation functions in the MD confirmed that the 50-MeV Si–induced tracks do not reach a vaporlike state. Thus the MD simulations also show that vaporization is not a prerequisite for the C/S track formation or the nanoparticle elongation.

VII. SUMMARY

One of the promising candidate mechanisms for the ion shaping of NPs is the thermal pressure model with elongation via underdense cores of the C/S tracks [20]. The cores and shells of the C/S tracks were once believed to be formed by the vaporization and melting of SiO_2, respectively (V-M model). To reexamine this model, ion tracks of SiO_2 formed by low-S_e irradiations, i.e., 60-MeV Ti (5.9 keV/nm) and 50-MeV Si (3.2 keV/nm), were evaluated by SAXS and compared with high-S_e irradiations (>10 keV/nm). Under the low-S_e irradiations of both 60-MeV Ti and 50-MeV Si, the formation of C/S tracks and the ion shaping of Zn nanoparticles were experimentally confirmed. The TT-MD simulations indicate from the pair distribution analysis that at least 50-MeV Si irradiation induces the melting transition, but not the vaporization. Even then, the simulations simultaneously reproduce the formation of C/S tracks and the ion shaping of NPs without the vaporization. Therefore, the V-M model is excluded. The C/S tracks are formed in SiO_2 without vaporization, probably due to the inhomogeneous radial temperature profile in a molten track [15]. The ion shaping of NPs is induced through mass transport via underdense cores of the tracks, in correlation with the recovery process of the silica matrix after emitting a pressure wave.

Therefore, the ion shaping of NPs is a phenomenon which includes the pressure effects and cannot be described by the conventional iTS model, i.e., a pair of coupled heat-diffusion equations which do not include the pressure effects.

ACKNOWLEDGMENTS

The SHI irradiations were performed under the Common-Use Facility Program of JAEA. H.A. was supported by JSPS-KAKENHI Grant No. 18K04898. I.S., V.J., F.D., and K.N. gratefully acknowledge financial support from the Academy of Finland MESIOS and NANOIS projects, and CPU capacity grants from the IT Centre for Science CSC in Espoo, Finland. Part of this work was performed at the SAXS/WAXS beamline at the Australian Synchrotron, part of ANSTO. P.K. acknowledges the Australian Research Council for financial support.

[1] R. L. Fleischer, P. B. Price, and R. M. Walker, J. Appl. Phys. **36**, 3645 (1965).
[2] N. Ishikawa, A. Iwase, Y. Chimi, O. Michikami, H. Wakana, and T. Kambara, J. Phys. Soc. Jpn. **69**, 3563 (2000).
[3] A. Benyagoub, Phys. Rev. B **72**, 094114 (2005).
[4] F. Seitz and J. S. Koehler, Solid State Phys. **2**, 305 (1956).
[5] M. Toulemonde, C. Dufour, and E. Paumier, Phys. Rev. B **46**, 14362 (1992).
[6] Ch. Dufour, V. Khomenkov, G. Rizza, and M. Toulemonde, J. Phys. D: Appl. Phys. **45**, 065302 (2012).
[7] N. Itoh, Nucl. Instrum. Methods Phys. Res., Sect. B **116**, 33 (1996).

[8] F. Agullo-López, A. Mendez, G. García, J. Olivares, and J. M. Cabrera, Phys. Rev. B **74**, 174109 (2006).

[9] A. A. Leino, S. L. Daraszewicz, O. H. Pakarinen, K. Nordlund, and F. Djurabekova, Europhys. Lett. **110**, 16004 (2015).

[10] T. van Dillen, E. Snoeks, W. Fukarek, C. M. van Kats, K. P. Velikov, A. van Blaaderen, and A. Polman, Nucl. Instrum. Methods Phys. Res., Sect. B **175-177**, 350 (2001).

[11] S. Klaumunzer, Nucl. Instrum. Methods Phys. Res., Sect. B **225**, 136 (2004).

[12] P. Kluth, C. S. Schnohr, O. H. Pakarinen, F. Djurabekova, D. J. Sprouster, R. Giulian, M. C. Ridgway, A. P. Byrne, C. Trautmann, D. J. Cookson *et al.*, Phys. Rev. Lett. **101**, 175503 (2008).

[13] P. Kluth, O. H. Pakarinen, F. Djurabekova, R. Giulian, M. C. Ridgway, A. P. Byrne, and K. Nordlund, J. Appl. Phys. **110**, 123520 (2011).

[14] K. Nakajima, Y. Morita, M. Suzuki, K. Narumi, Y. Saitoh, N. Ishikawa, K. Hojou, M. Tsujimoto, S. Isoda, and K. Kimura, Nucl. Instrum. Methods Phys. Res., Sect. B **291**, 12 (2012).

[15] P. Mota-Santiago, H. Vazquez, T. Bierschenk, F. Kremer, A. Nadzri, D. Schauries, F. Djurabekova, K. Nordlund, C. Trautmann, S. Mudie *et al.*, Nanotechnology **29**, 144004 (2018).

[16] C. D'Orleans, J. P. Stoquert, C. Estournès, C. Cerruti, J. J. Grob, J. L. Guille, F. Haas, D. Muller, and M. Richard-Plouet, Phys. Rev. B **67**, 220101 (2003).

[17] S. Roorda, T. van Dillen, A. Polman, C. Graf, A. van Blaaderen, and B. J. Kooi, Adv. Mater. **16**, 235 (2004).

[18] M. C. Ridgway, R. Giulian, D. J. Sprouster, P. Kluth, L. L. Araujo, D. J. Llewellyn, A. P. Byrne, F. Kremer, P. F. P. Fichtner, G. Rizza *et al.*, Phys. Rev. Lett. **106**, 095505 (2011).

[19] C. Harkati Kerboua, J. M. Lamarre, M. Chicoine, L. Martinu, and S. Roorda, Thin Solid Films **527**, 186 (2013).

[20] A. A. Leino, O. H. Pakarinen, F. Djurabekova, K. Nordlund, P. Kluth, and M. C. Ridgway, Mater. Res. Lett. **2**, 37 (2014).

[21] H. Amekura, N. Okubo, D. Tsuya, and N. Ishikawa, AIP Adv. **7**, 085304 (2017).

[22] H. Amekura, S. Mohapatra, U. B. Singh, S. A. Khan, P. K. Kulriya, N. Ishikawa, N. Okubo, and D. K. Avasthi, Nanotechnology **25**, 435301 (2014).

[23] P. Kluth, C. S. Schnohr, D. J. Sprouster, A. P. Byrne, D. J. Cookson, and M. C. Ridgway, Nucl. Instrum. Methods Phys. Res., Sect. B **266**, 2994 (2008).

[24] M. P. Allen and D. J. Tildesley, *Computer Simulation of Liquids* (Oxford University Press, Oxford, UK, 1989).

[25] K. Nordlund, PARCAS computer code (2016). The main principles of the molecular dynamics algorithms are presented in [25,26]. The adaptive time step and electronic stopping algorithms are the same as in [27].The code is published as part of [28].

[26] K. Nordlund, M. Ghaly, R. S. Averback, M. Caturla, T. Diaz de la Rubia, and J. Tarus, Phys. Rev. B **57**, 7556 (1998).

[27] M. Ghaly, K. Nordlund, and R. S. Averback, Philos. Mag. A **79**, 795 (1999).

[28] K. Nordlund, Comput. Mater. Sci. **3**, 448 (1995).

[29] F. Granberg, K. Nordlund, M. W. Ullah, K. Jin, C. Lu, H. Bei, L. M. Wang, F. Djurabekova, W. J. Weber, and Y. Zhang, Phys. Rev. Lett. **116**, 135504 (2016).

[30] K. Nordlund, M. Ghaly, and R. S. Averback, J. Appl. Phys. **83**, 1238 (1998).

[31] A. A. Leino, O. H. Pakarinen, F. Djurabekova, and K. Nordlund, Nucl. Instrum. Methods Phys. Res., Sect. B **282**, 76 (2012).

[32] H. Vázquez, E. H. Åhlgren, O. Ochedowski, A. A. Leino, R. Mirzayev, R. Kozubek, H. Lebius, M. Karlušic, M. Jakšic, A. V. Krasheninnikov *et al.*, Carbon **114**, 511 (2017).

[33] M. Toulemonde, W. Assmann, C. Dufour, A. Meftah, F. Studer, and C. Trautmann, Mat. Fys. Medd. Kong. Dan. Vidensk. Selsk. **52**, 263 (2006).

[34] O. H. Pakarinen, F. Djurabekova, and K. Nordlund, Nucl. Instrum. Methods Phys. Res., Sect. B **268**, 3163 (2010).

[35] F. Djurabekova and K. Nordlund, Phys. Rev. B **77**, 115325 (2008).

[36] S. M. Foiles, M. I. Baskes, and M. S. Daw, Phys. Rev. B **33**, 7983 (1986).

[37] S. M. Foiles, M. I. Baskes, and M. S. Daw, Phys. Rev. B **37**, 10378 (1988).

[38] T. Watanabe, D. Yamasaki, K. Tatsumura, and I. Ohdomari, Appl. Surf. Sci. **234**, 207 (2004).

[39] J. Samela, K. Nordlund, V. N. Popok, and E. E. B. Campbell, Phys. Rev. B **77**, 075309 (2008).

[40] S. Munetoh, T. Motooka, K. Moriguchi, and A. Shintani, Comput. Mater. Sci. **39**, 334 (2007).

[41] P. Erhart, N. Juslin, O. Goy, K. Nordlund, R. Müller, and K. Albe, J. Phys.: Condens. Matter **18**, 6585 (2006).

[42] M. Toulemonde, W. J. Weber, G. Li, V. Shutthanandan, P. Kluth, T. Yang, Y. Wang, and Y. Zhang, Phys. Rev. B **83**, 054106 (2011).